

# Terahertz emission from two-dimensional Ruddlesden-Popper halide perovskites driven by electric dipole and quadrupole under below-band-gap excitation

Huizhu Li<sup>1</sup>,<sup>✉</sup> Yixuan Zhou<sup>1,\*</sup>, Yayan Xi<sup>1</sup>, Yongqiang Zou<sup>1</sup>, Zhen Lei<sup>1</sup>, Xueqin Cao<sup>1</sup>, Yuanyuan Huang,<sup>1</sup> Dehui Li,<sup>2,†</sup> and Xinlong Xu<sup>1,‡</sup>

<sup>1</sup>*Shaanxi Joint Lab of Graphene, State Key Lab Incubation Base of Photoelectric Technology and Functional Materials, International Collaborative Center on Photoelectric Technology and Nano Functional Materials, Institute of Photonics & Photon-Technology, School of Physics, Northwest University, Xi'an 710069, China*

<sup>2</sup>*School of Optical and Electronic Information, Huazhong University of Science and Technology, Wuhan 430074, China*



(Received 14 August 2023; revised 14 November 2023; accepted 20 November 2023; published 5 December 2023)

Understanding the nonlinear polarization mechanism of two-dimensional (2D) halide perovskites is essential for developing various nonlinear optical applications. Herein, the terahertz (THz) emission from Ruddlesden-Popper type  $(\text{BA})_2\text{PbI}_4$  and  $(\text{iso-BA})_2\text{PbI}_4$  are investigated by both above-band-gap (400 nm) and below-band-gap (800 nm) femtosecond laser excitation. Under above-band-gap excitation, the dominant mechanism is the linear photogalvanic effect instead of the common photo-Dember effect and surface depletion field effect, suggesting the carrier transport between adjacent conductor layers is forbidden by the organic layers. Under below-band-gap excitation, the THz emission from orthorhombic  $(\text{BA})_2\text{PbI}_4$  exhibits a remarkable quadruple rotational symmetry on the azimuthal angle, indicating that the nonlinear polarization is driven by a higher-order electric quadrupole term instead of the bulk electric dipole term, which is forbidden by the centrosymmetric structure. In comparison, the low symmetry of THz emission on the azimuthal angle of monoclinic  $(\text{iso-BA})_2\text{PbI}_4$  is attributed to the influence of symmetry breaking in the surface region, which raises a surface electric dipole contribution. In this paper, we reveal THz emission spectroscopy as a powerful contactless technique in investigating the nonlinear polarization of advanced materials.

DOI: [10.1103/PhysRevB.108.245403](https://doi.org/10.1103/PhysRevB.108.245403)

## I. INTRODUCTION

Two-dimensional (2D) halide Ruddlesden-Popper perovskites (RPPs) have attracted growing interest due to their superior environmental stability [1–3] and unique optoelectronic properties [4–6] compared with their three-dimensional (3D) analogs.  $(\text{BA})_2\text{PbI}_4$  (BA: butylammonium) is one of the most extensively studied RPPs [7,8] due to its simple preparation process [9], good stability [10], and rich excitonic photophysics [11]. Consequently, it finds wide applications in solar cells [12,13], photodetectors [14], light-emitting diodes [15], and various other optoelectronic devices [16]. Structurally,  $(\text{BA})_2\text{PbI}_4$  can be regarded as cleaving the 3D structure along a crystallographic plane into separated 2D octahedral  $[\text{PbI}_6]^{4-}$  layers, which are spaced by two sizeable organic cation  $\text{BA}^+$  layers [17]. Furthermore, there exists an isomer of  $(\text{BA})_2\text{PbI}_4$  denoted as  $(\text{iso-BA})_2\text{PbI}_4$ , which can be obtained by replacing the linear  $n\text{-BA}^+$  chains with short branched  $\text{iso-BA}^+$  (isobutylammonium) chains and exhibits similar physical and chemical properties [17]. However, their crystal systems differ due to distinct structural arrangement [8,18]. The incorporation of organic spacers in 2D RPPs results in the formation of a multiple-quantum-

well structure consisting of stacked semiconductor/insulator layers [19]. This introduces remarkable quantum [20] and dielectric confinement [8,21,22] effects, which are closely associated with their exceptional nonlinear optical properties and diverse applications such as up-conversion photoluminescence (PL) for imaging [23], multiphoton pumped lasers [24], sub-band-gap and self-powered photodetectors [25,26] as well as electro-optic and all-optical modulators [27,28]. However, a comprehensive understanding of the nonlinear polarization mechanism in 2D RPPs, which exhibits high sensitivity to structural variations, remains elusive.

Second-order nonlinear optical frequency mixing is the earliest studied and most widely used nonlinear optical process. With a single-frequency light excitation, the second-order polarization will be divided into the second harmonic generation (SHG) term and a direct current (DC) polarization term, which is known as the optical rectification effect [29]. The experimental approach of SHG has been widely used in studying the intrinsic symmetry of materials, the symmetry breaking on the surface, and even the higher-order electric quadrupole contribution [30]. In comparison, the emission photons of the optical rectification effect have a central frequency in the terahertz (THz) region, which enables the emerging THz emission spectroscopy, another powerful contactless optical technique, to investigate the nonlinear polarization sources of materials [31].

THz emission spectroscopy has proven successful in investigating the ultrafast changes of charge carriers [32,33]

\*Corresponding author: yxzhou@nwu.edu.cn

†Corresponding author: dehuili@hust.edu.cn

‡Corresponding author: xlxuphy@nwu.edu.cn

and polarons [34] as well as the transient photocurrents induced by linear and circular photogalvanic effects in 3D perovskites [35–39]. A study has been conducted to research the spin-orbit-coupling-induced circular photogalvanic effect in 2D perovskites of  $(\text{C}_6\text{H}_5(\text{CH}_2)_2\text{NH}_3)_2\text{PbI}_4$  [39]. However, the mechanisms of transient photocurrent and nonlinear polarization, which can offer broader insights into THz generation excited by linearly polarized lasers, remain largely unexplored for 2D perovskites. Moreover, it remains unclear whether and how nonlinear polarization influences the THz generation in perovskites, including their 3D analogs. For instance, under above-band-gap excitation, the THz generation in  $\text{MAPbI}_3$  and  $\text{FAPbI}_3$  is primarily governed by the photo-Dember effect [32,34], surface depletion field effect [33], and polarons [34]. Even in our previous study involving below-band-gap excitation, the dominant mechanism for THz generation in  $\text{CsPbBr}_3$  excited by an 800 nm laser was found to be two-photon absorption-induced shift current rather than second-order nonlinear polarization [37,38]. Therefore, we select 2D RPPs  $(\text{BA})_2\text{PbI}_4$  and  $(\text{iso-BA})_2\text{PbI}_4$  with the expectation of observing definite nonlinear polarization-related THz generation phenomena due to their enhanced nonlinear optical properties in comparison with 3D perovskites. Additionally, the distinct structural arrangement of these two RPPs, which are composed of the same elements, provides a promising platform for investigating various sources of nonlinear polarization in 2D perovskites, such as microscopic dipole and quadrupole moments. These phenomena are fundamentally significant but have received relatively less exploration.

In this paper, the THz emission spectroscopy of  $(\text{BA})_2\text{PbI}_4$  and  $(\text{iso-BA})_2\text{PbI}_4$  is investigated, employing laser excitation conditions at 400 and 800 nm wavelengths. According to the linear dependence of the THz electric field on the pump fluence, the THz generation mechanisms can be assigned to the optical rectification and linear photogalvanic effects under below- and above-band-gap excitation conditions, respectively. From the dependence of THz emission on the pump incident angle, pump polarization angle, and sample azimuthal angle, nonlinear polarization of  $(\text{BA})_2\text{PbI}_4$  and  $(\text{iso-BA})_2\text{PbI}_4$  are demonstrated to have different polarization sources. The remarkable quadruple rotational symmetry of orthorhombic  $(\text{BA})_2\text{PbI}_4$  on azimuthal angle implies the influence of an electric quadrupole term. In comparison, the low symmetry of  $(\text{iso-BA})_2\text{PbI}_4$  could be attributed to the surface electric dipole related to the monoclinic structure.

## II. EXPERIMENT

### A. Sample preparation and characterization

$(\text{BA})_2\text{PbI}_4$  and  $(\text{iso-BA})_2\text{PbI}_4$  single-crystal flakes were synthesized by a solution method as reported previously [7,40]. The *n*-butylammonium iodide (BAI) solution was synthesized by mixing an *n*- $\text{CH}_3(\text{CH}_2)_3\text{NH}_2$  (924  $\mu\text{L}$ , 10 mmol) and a 57% w/w aqueous HI (5 mL, 38 mmol) under stirring at 0 °C for 4 h. For the synthesis of  $(\text{BA})_2\text{PbI}_4$ ,  $\text{PbO}$  powder (2232 mg, 10 mmol) was dissolved in a mixture of 57% w/w aqueous HI solution (10.0 mL, 76 mmol) and 50% aqueous  $\text{H}_3\text{PO}_2$  (1.7 mL, 15.5 mmol) by heating to boiling under a constant magnetic stirring for  $\sim 5$  min. Addition of

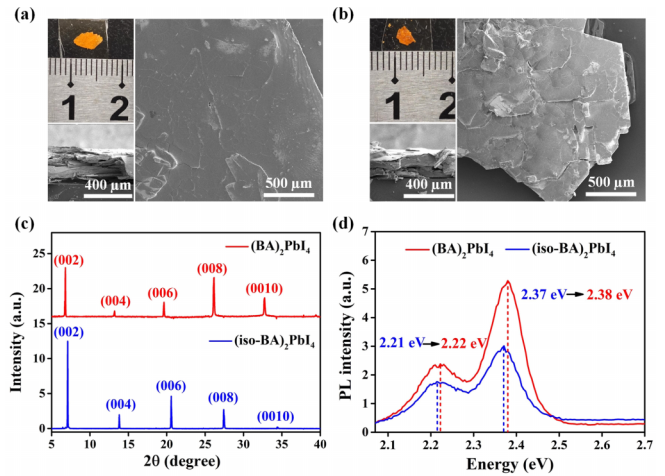


FIG. 1. Characterization of two-dimensional (2D) perovskites. (a) Photograph and scanning electron microscopy (SEM) images of a  $(\text{BA})_2\text{PbI}_4$  single-crystal flake. (b) Photograph and SEM images of a  $(\text{iso-BA})_2\text{PbI}_4$  single-crystal flake. (c) X-ray diffraction (XRD) patterns of  $(\text{BA})_2\text{PbI}_4$  (red line) and  $(\text{iso-BA})_2\text{PbI}_4$  (blue line) single-crystal flakes. (d) Photoluminescence (PL) spectra of  $(\text{BA})_2\text{PbI}_4$  (red line) and  $(\text{iso-BA})_2\text{PbI}_4$  (blue line) single-crystal flakes.

the *n*-BAI solution to the  $\text{PbI}_2$  solution initially produced a black precipitate, which was subsequently dissolved when the solution is reheated to boil. The stirring was then discontinued, and the solution was left to cool to room temperature; during this time, the orange rectangular plates began to crystallize. The precipitation was deemed to be complete after  $\sim 2$  h. The crystals were isolated by suction filtration and thoroughly dried under reduced pressure. For the synthesis of  $(\text{iso-BA})_2\text{PbI}_4$  single crystal, the same procedure was used except that the linear *n*-BA was replaced by its isomer short branched iso-BA. In the THz emission measurements, the single-crystal flakes were affixed onto the sapphire substrate using polymethyl methacrylate (PMMA) as the adhesive due to the impracticality of measuring the sample under self-supporting conditions. Additionally, a layer of PMMA was applied on the top surface of the sample to prevent moisture and oxidation. It should be noted that neither PMMA nor the sapphire substrate contribute to the THz generation experiment, as demonstrated in Fig. S1 in the Supplemental Material [41].

The morphologies of  $(\text{BA})_2\text{PbI}_4$  and  $(\text{iso-BA})_2\text{PbI}_4$  single-crystal flakes were characterized by scanning electron microscopy (SEM, Thermo Fisher, Apero s) and optical photographs, as shown in Figs. 1(a) and 1(b), respectively. From the inset photographs as given on the upper left, both single-crystal flakes exhibit bright orange color and plate shape with a size of several millimeters. The main figures on the right show the top-view SEM images of the samples, which reveal smooth surfaces. The illustrations at the bottom left (side-view SEM image) demonstrate approximate thicknesses ranging from 300 to 350  $\mu\text{m}$  and exhibit clear layered structures. These morphological results are identical to the literature [18].

The crystallinity and growth orientation characteristics of  $(\text{BA})_2\text{PbI}_4$  and  $(\text{iso-BA})_2\text{PbI}_4$  flakes were resolved via x-

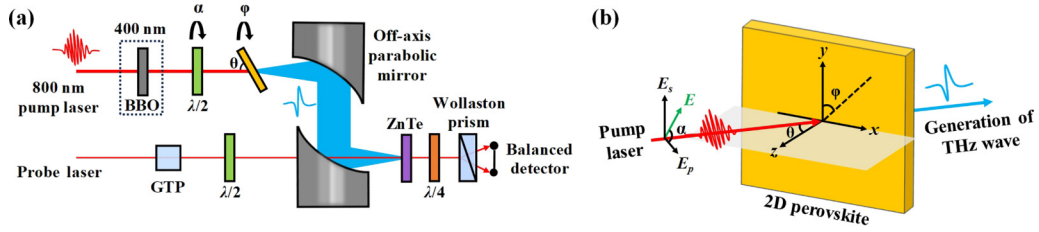


FIG. 2. Schematic illustration of the terahertz (THz) emission measurements. (a) THz spectroscopy setup with 800 nm and switchable 400 nm excitation configurations.  $\beta$ -BBO: beta barium borate crystal. GTP: Glan-Taylor prism.  $\lambda/2$ : half-wave plate (HWP).  $\lambda/4$ : quarter-wave plate (QWP). (b) THz emission from a two-dimensional (2D) perovskite sample excited by a femtosecond laser.  $xyz$  represents the crystal coordinate.  $\alpha$ ,  $\theta$ , and  $\varphi$  represent the polarized angle of the pump light, the incidence angle of the pump light, and the azimuthal angle of the sample, respectively.

ray diffraction (XRD, Bruker, D8 Advance), as shown in Fig. 1(c). For the red curve, the diffraction peaks located at  $6.75^\circ$ ,  $3.2^\circ$ ,  $19.6^\circ$ ,  $26.16^\circ$ , and  $32.76^\circ$  correspond to the (002), (004), (006), (008), and (0010) crystal planes of the  $(\text{BA})_2\text{PbI}_4$  single crystal, respectively. The peak positions match well with the previous report [7, 18], which are assigned to the orthorhombic crystal phase with a  $Pcba$  space group [8]. Moreover, the diffraction peaks are exclusively associated with the (001) crystallographic family of planes [8], revealing that the  $(\text{BA})_2\text{PbI}_4$  single crystal preferentially grows along the [110] direction, and the  $[\text{PbI}_6]^{4-}$  layer is parallel to the substrate [42]. The black line shows the XRD pattern of the (iso- $\text{BA})_2\text{PbI}_4$  single crystal, the diffraction peaks are indexed to the monoclinic structure with a  $P2_1/C$  space group, and the sharp peak shape reflects an excellent crystalline quality [18]. In comparison with those of  $(\text{BA})_2\text{PbI}_4$ , the diffraction peaks of (iso- $\text{BA})_2\text{PbI}_4$  locate at higher angles, indicating a narrower interplanar spacing [43].

Figure 1(d) shows the PL spectra of these RPP single crystals measured using a fluorescence spectrophotometer (Rili, F-7000) excited by a 450 nm laser. For  $(\text{BA})_2\text{PbI}_4$ , two emission peaks can be observed at 2.22 eV (558 nm) and 2.38 eV (521 nm). The peak with higher energy is attributed to the excitonic emission in individual 2D layers and is independent of the interlayer interaction, while the lower-energy peak originates from the interlayer electronic interaction [44, 45]. Similarly, two emission peaks located at 2.21 eV (561 nm) and 2.37 eV (523 nm) can be observed in (iso- $\text{BA})_2\text{PbI}_4$ . Both peaks are slightly redshifted compared with those of  $(\text{BA})_2\text{PbI}_4$ , originating from the shortening of the carbon chain [46], which reduces the interlayer spacing and strengthens the electronic interaction.

### B. THz emission experimental setup

The schematic of the THz emission spectroscopy system is shown in Fig. 2. A Ti:sapphire femtosecond laser regenerated amplifier (Spectra-Physics, Spitfire) produces the laser pulse with a central wavelength of 800 nm, a duration of 35 fs, and a repetition rate of 1 kHz. The laser beam is split into pump and probe beams. The pump beam carrying most of the energy is focused onto the sample with a spot of  $\sim 3$  mm in diameter. In this transmission excitation configuration, the incident angle can be tuned from  $-40^\circ$  to  $40^\circ$  by rotating the sample holder. For 400 nm excitation, the pump laser is doubled by a  $\beta$ -BBO crystal. The resulting THz field is focused by a pair of

parabolic mirrors onto a detection crystal ZnTe. Meanwhile, the probe beam with a small amount of energy is also focused onto the ZnTe detection crystal collinearly. The time-domain THz waveform can be obtained by the electro-optic sampling principle with the help of a balanced detector. In addition, the linear polarization states of the pump beam can be tuned by a half-wave plate (HWP), which is installed in front of the sample.

Figure 2 also exhibits the schematic diagram of the THz emission process from layered RPPs excited by ultrafast laser. The horizontal ( $p$ ) and vertical ( $s$ ) polarization of the incident beam are aligned along the  $E_p$  and  $E_s$  axes, respectively. The polarization angle  $\alpha$  of the pump laser can be controlled by the HWP. The azimuthal angle  $\varphi$  can be tuned from  $0^\circ$  to  $360^\circ$  by rotating the sample around the  $z$  axis. The incident angle  $\theta$  is between the incident light vector and the normal direction of the surface.

## III. RESULTS AND DISCUSSIONS

THz emission measurements are conducted on  $(\text{BA})_2\text{PbI}_4$  and (iso- $\text{BA})_2\text{PbI}_4$  under oblique incidence excitation at  $-40^\circ$  using lasers at wavelengths of 400 and 800 nm. The pump fluence is set to  $0.57 \text{ mJ/cm}^2$  for the 800 nm excitation and  $0.64 \text{ mJ/cm}^2$  for the 400 nm excitation. Figure 3(a) shows the THz time-domain signals of  $(\text{BA})_2\text{PbI}_4$  on a sapphire substrate excited by 400 nm lasers. Note that the difference between  $p$ - and  $s$ -polarized excitation conditions cannot be well distinguished due to the low ratio of signal to noise, so the THz signal here is measured without using HWP. Nevertheless, the THz amplitude under 400 nm excitation is weaker than that under 800 nm excitation. For 400 nm excitation, the photon energy of 3.1 eV is larger than the band-gap energy of 2.38 eV so that real photocarriers can be produced. Therefore, the photocurrent could become the source of the generated THz electric field under 400 nm laser excitation.

In comparison, the THz emission spectrum of  $(\text{BA})_2\text{PbI}_4$  under  $p$ - and  $s$ -polarized 800 nm lasers excitation is shown in Fig. 3(b). A clear peak-valley structure of the THz waves can be observed for both  $p$ - and  $s$ -polarized excitation conditions, and the amplitude under  $p$ -polarized excitation is  $\sim 1.8$  times as much as that under  $s$ -polarized excitation. In general, THz emission from nonmagnetic semiconductors under ultrafast laser excitation is related to the time-varying nonlinear polarization ( $P$ ) and photocurrent density ( $J$ ) as [47]  $\mathbf{E}_{\text{THz}} \propto \partial^2 \mathbf{P} / \partial t^2 + \partial \mathbf{J} / \partial t$ . For 800 nm excitation, the

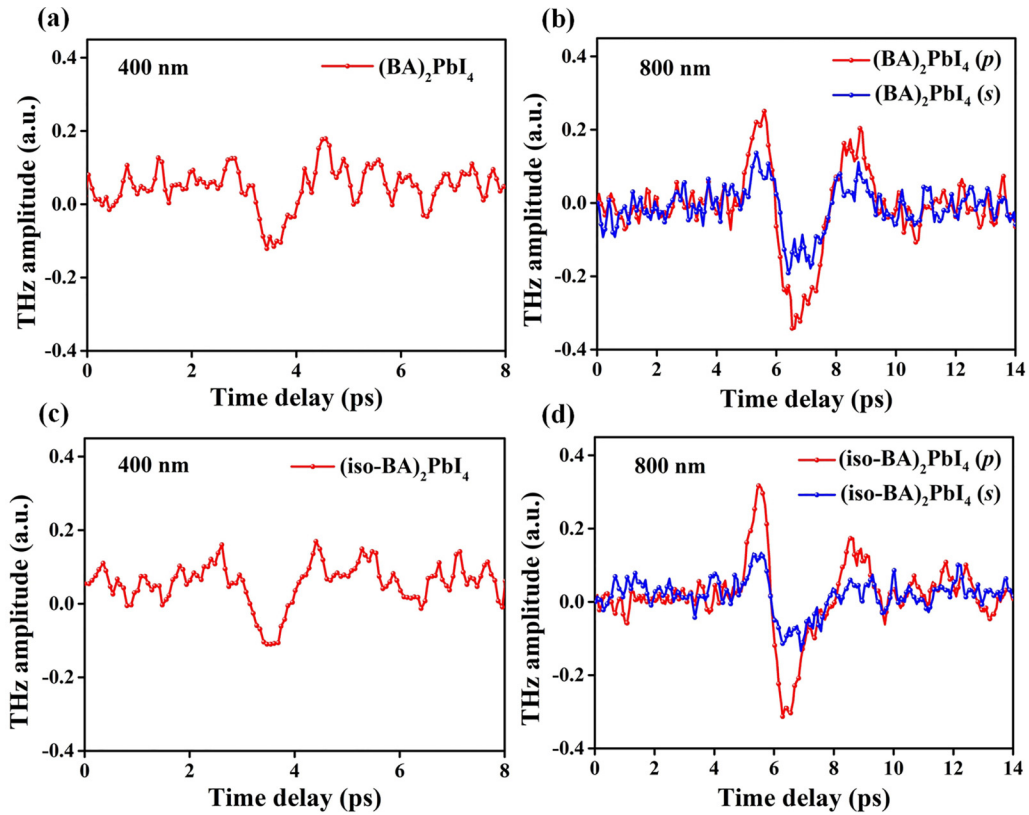


FIG. 3. Terahertz (THz) time-domain signals are generated from two-dimensional (2D) perovskites. (a) THz waves from  $(\text{BA})_2\text{PbI}_4$  under  $p$ - and  $s$ -polarized laser excitation at 400 nm. (b) THz wave from  $(\text{BA})_2\text{PbI}_4$  under 800 nm laser excitation. (c) THz waves from  $(\text{iso-BA})_2\text{PbI}_4$  under  $p$ - and  $s$ -polarized laser excitation at 400 nm. (d) THz wave from  $(\text{iso-BA})_2\text{PbI}_4$  under 800 nm laser excitation.

photon energy of 1.55 eV is far below the band-gap energy (2.38 eV) of  $(\text{BA})_2\text{PbI}_4$  and no photogenerated carriers can be induced [18,48]. Therefore, nonlinear polarization should dominate the THz generation under 800 nm excitation.

The THz emission signals of  $(\text{iso-BA})_2\text{PbI}_4$  under the excitation of 400 and 800 nm lasers are shown in Figs. 3(c) and 3(d), respectively. The amplitude and shape of the THz pulses are like those of  $(\text{BA})_2\text{PbI}_4$ . With the band-gap energy of 2.37 eV, the THz radiation from  $(\text{iso-BA})_2\text{PbI}_4$  under above-band-gap excitation could also be attributed to the transient photocurrent, while under below-band-gap excitation, it could be attributed to the nonlinear polarization.

From the above results, an unusual phenomenon is that the THz signals from both  $(\text{BA})_2\text{PbI}_4$  and  $(\text{iso-BA})_2\text{PbI}_4$  are suppressed under 400 nm excitation. Note that the transient photocurrents induced by the photo-Dember effect and surface depletion field effect have been reported to be the dominant mechanisms for the THz emission from 3D perovskites such as  $\text{MAPbI}_3$  [32],  $\text{FAPbI}_3$  [33], and  $\text{MAPbBr}_2$  [36]. However, the nonlinear polarization seems to be more significant for these 2D RPPs measured here. In the following part, we further evaluate the physical mechanisms of THz radiation under 400 and 800 nm excitation by measuring the dependence of THz amplitude on the pump fluence.

Figure 4(a) shows the peak-to-valley amplitude of the THz pulse generated from  $(\text{BA})_2\text{PbI}_4$  excited by 400 and 800 nm lasers as a function of pump fluence. The pump laser in the experiment is consistently maintained in a  $p$ -polarization state,

with an incident angle of  $-40^\circ$ . For 400 nm excitation, the THz amplitude increases linearly with the rise of the pump fluence from 0.255 to 0.830  $\text{mJ}/\text{cm}^2$  with a slope of 0.36. For 800 nm excitation, the same linear dependence of the pump fluence is observed in the range of 0.283-0.707  $\text{mJ}/\text{cm}^2$ , and the slope is 0.88. The linear dependence suggests that the THz radiation mechanisms of  $(\text{BA})_2\text{PbI}_4$  for both excitation conditions can be assigned to the second-order nonlinear process. For the above-band-gap excitation condition with 400 nm laser, the second-order nonlinear process could be related to the photogalvanic effect or the photon drag effect, which contributes a time-varying photocurrent for the THz generation [49]. To distinguish between these two effects, THz waves generated under two opposite illumination directions have been measured. The polarity of the THz wave vector is found identical under the excitation from the front and back sides, suggesting that the photogalvanic effect should be the dominant mechanism. It is worth noting that no saturation phenomenon, typically arising from the electrostatic screening effect of highly accumulated photogenerated carriers, is observed even in the high pump fluence region. This observation suggests that linear optical processes such as the photo-Dember effect and surface depletion field effect, which are crucial in 3D perovskites like  $\text{MAPbI}_3$  [32,33], can be excluded as dominant mechanisms. For the below-band-gap excitation condition with 800 nm laser, the second-order nonlinear process generally refers to the contribution of optical rectification, in which the nonlinear polarization dominates.

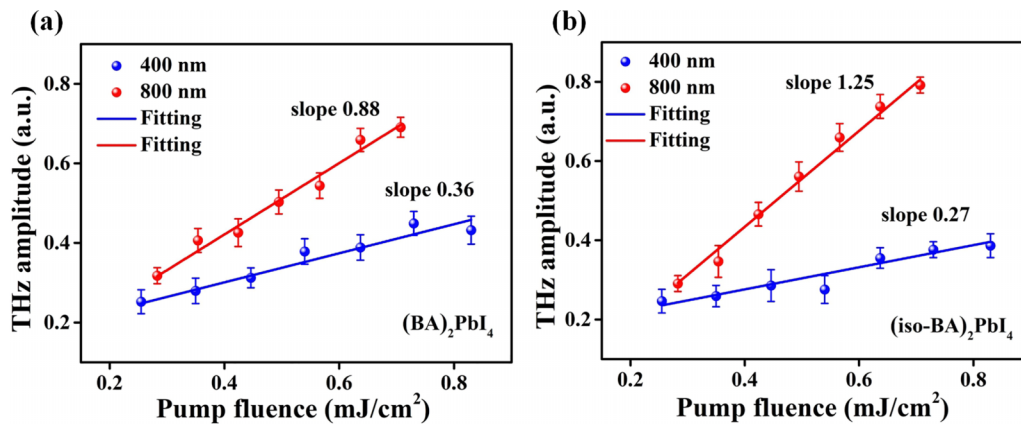


FIG. 4. Pump fluence dependence of the terahertz (THz) amplitude from (a)  $(\text{BA})_2\text{PbI}_4$  and (b)  $(\text{iso-BA})_2\text{PbI}_4$  under 400 nm (blue) and 800 nm (red) laser excitation. The dots are experimental data, and the lines are linear fitting.

Similar linear dependence can be obtained for  $(\text{iso-BA})_2\text{PbI}_4$  as exhibited in Fig. 4(b), indicating that the THz generation is also dominated by second-order nonlinear processes. Moreover, under 400 and 800 nm excitation conditions, the slope values are 0.27 and 1.25, respectively. For both  $(\text{BA})_2\text{PbI}_4$  and  $(\text{iso-BA})_2\text{PbI}_4$ , the greatly reduced THz amplitude and pump-fluence-dependent slope under above-band-gap excitation suggest that the photocurrent is largely suppressed. These unusual phenomena could be originated from the unique structure of 2D perovskites.

In the lattice of 2D RPPs, the conducting  $[\text{MX}_6]^{4-}$  layers are spaced by insulating organic layers, which form a multiple-quantum-well structure. On the one hand, in the direction perpendicular to the  $[\text{MX}_6]^{4-}$  layer, the carrier transport between adjacent conductor layers is largely restricted by the organic spacers, which further decreases carrier mobility, enhances charge accumulation, and increases radiative recombination losses [17]. According to the SEM and XRD results, the  $[\text{PbI}_6]^{4-}$  layers in both  $(\text{BA})_2\text{PbI}_4$  and  $(\text{iso-BA})_2\text{PbI}_4$  samples are parallel to the substrate surface. Consequently, this alignment significantly suppresses the linear transient photocurrents induced by the photo-Dember electric field and surface depletion electric field, which are perpendicular to the conducting layers. On the other hand, the quantum well effect formed by this crystal structure restricts the organic cations to the organic layer and the anions to the inorganic layer. The 2D layer of the positively charged amine group combines with the adjacent layer of negatively charged iodide ions to form a polar surface between the organic and inorganic layers. The resulting polarization is stronger than the photocurrent in the direction perpendicular to the sample surface [50]. Therefore, the optical rectification effect governing THz emission of 2D perovskites under 800 nm excitation is much more remarkable than the photocurrent dominated THz generation excited by the 400 nm laser.

In the following part, the nonlinear polarization-dominated THz generation mechanisms of  $(\text{BA})_2\text{PbI}_4$  and  $(\text{iso-BA})_2\text{PbI}_4$  excited by 800 nm laser are investigated by changing the incident angle, polarization angle of the pump laser, and azimuthal angle. When not utilized as a variable, the pump laser is consistently maintained in a  $p$ -polarization

state with a fluence of  $0.57 \text{ mJ/cm}^2$  and an incident angle of  $-40^\circ$ . Figures 5(a) and 5(b) show the incident angle dependence of the THz peak-to-valley amplitude emitted from  $(\text{BA})_2\text{PbI}_4$  and  $(\text{iso-BA})_2\text{PbI}_4$ , respectively. Generally, the THz emission is weak at normal incidence while becoming stronger with the rise of incident angle up to  $\pm 40^\circ$ . Moreover, the polarity of THz amplitude is reversed at opposite incident angles. For the  $(\text{iso-BA})_2\text{PbI}_4$  sample, it should be noted that the fitting line is shifted to the positive side compared with the symmetrically distributed line of  $(\text{BA})_2\text{PbI}_4$ , implying different possible sources of nonlinear polarization.

Figures 5(c) and 5(d) show the polarization angles of the pump laser dependence of THz radiation from  $(\text{BA})_2\text{PbI}_4$  and  $(\text{iso-BA})_2\text{PbI}_4$  with an incidence angle of  $-40^\circ$ , respectively. For both samples, the THz amplitude exhibits a twofold rotational symmetry to the polarization angle, with the maximum values located at  $0^\circ$ ,  $180^\circ$ , and  $360^\circ$  and the minimum values at  $90^\circ$  and  $270^\circ$ . Therefore, fitting lines calculated with a  $\cos 2\alpha$  dependence agree well with the experiments. According to the polarization angle dependence of many reported semiconductors [51–53], the twofold rotational symmetry could be regarded as proof of the existence of nonlinear optical mechanisms. This result further supports the conclusion drawn from the pump power dependence of the two samples. However, the source of the nonlinear optical process cannot be distinguished here.

Further, the dependence of THz radiation on the azimuthal orientation  $\varphi$ , which is closely related to the crystal symmetry and second-order nonlinear susceptibility, is measured as shown in Figs. 5(e) and 5(f). Under  $p$ -polarization excitation, the THz amplitude emitted from  $(\text{BA})_2\text{PbI}_4$  as a function of  $\varphi$  at  $\theta = -40^\circ$  is exhibited in Fig. 5(e). Several maximum values are observed at  $90^\circ$ ,  $180^\circ$ ,  $270^\circ$ , and  $360^\circ$  by rotating the azimuthal angle from  $0^\circ$  to  $360^\circ$ , which presents a quadruple rotation symmetry. In comparison, the azimuthal angle dependence of THz radiation from  $(\text{iso-BA})_2\text{PbI}_4$  at the fixed incident angle of  $-40^\circ$  is shown in Fig. 5(f). The maximum THz radiation amplitude is observed at  $210^\circ$ , and another inconspicuous THz peak is  $\sim 30^\circ$ . This anisotropy dependence of THz amplitude appears as a combination of onefold and twofold rotational symmetry. The dramatically different az-

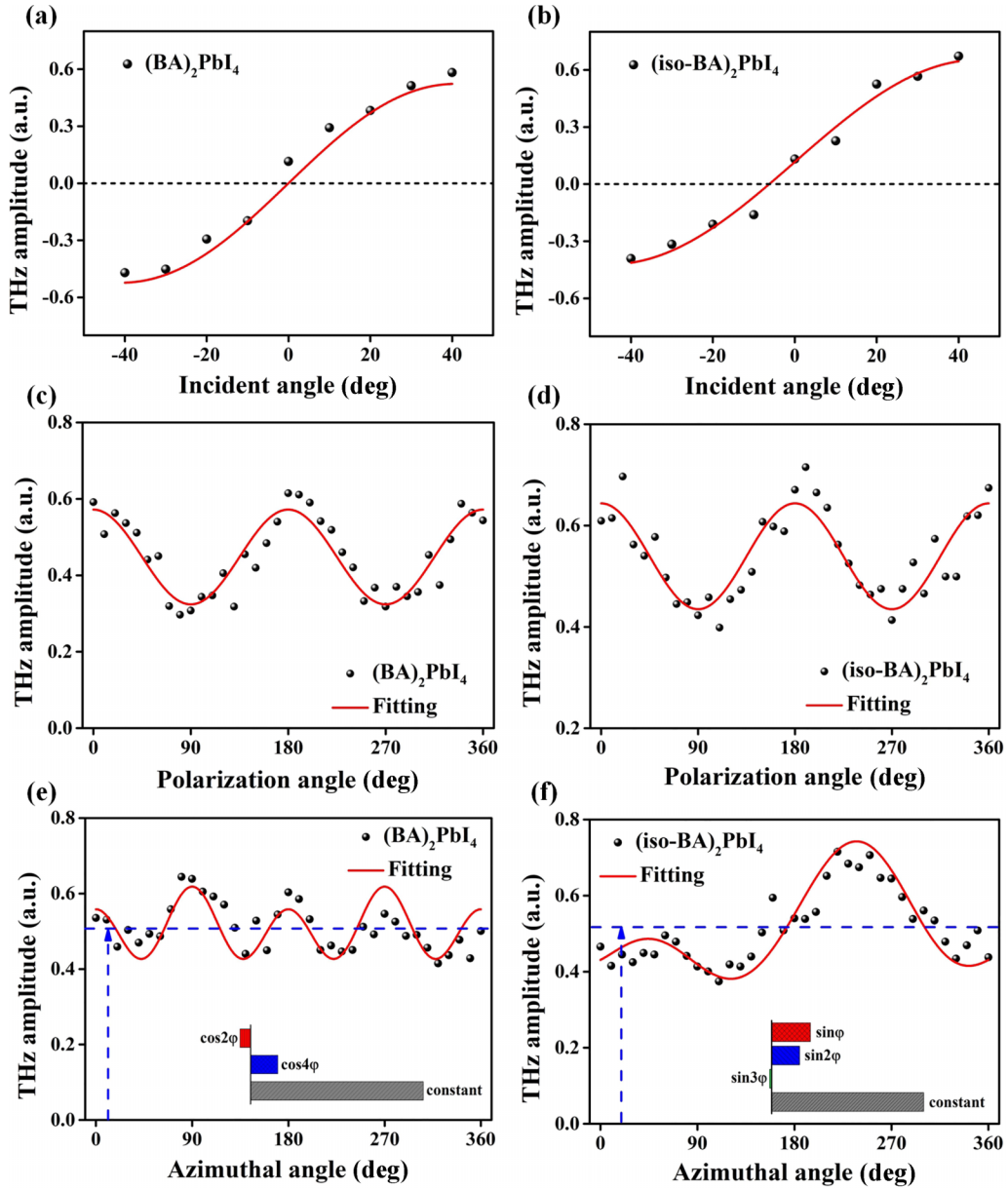


FIG. 5. The incident angle, polarization angle of the pump laser, and azimuthal angle dependent terahertz (THz) peak-to-valley amplitude of  $(\text{BA})_2\text{PbI}_4$  and  $(\text{iso-BA})_2\text{PbI}_4$  under 800 nm excitation. (a) and (b) THz amplitude as a function of the incident angle. (c) and (d) THz amplitude as a function of the polarization angle. (e) and (f) THz amplitude as a function of azimuthal angle. The experimental and fitting results are depicted with black dots and red solid lines. The blue arrow indicates the amplitude shift from zero baselines. The insets of (e) and (f) show the proportion of each term in the fitting formula.

imuthal angle dependence of  $(\text{BA})_2\text{PbI}_4$  and  $(\text{iso-BA})_2\text{PbI}_4$  serves as the final proof for the distinct sources of their non-linear polarization.

The THz emission induced by optical rectification depends on the second-order polarization of materials. As a nonlinear difference frequency mixing process, the optical rectification effect has a general nonlinear source polarization on the form [54]:

$$\mathbf{P}^{(2)}(\Omega = \omega - \omega) = \mathbf{P}_d^{(2)}(\Omega) + \mathbf{P}_s^{(2)}(\Omega) + \mathbf{P}_q^{(2)}(\Omega) + \dots, \quad (1)$$

where  $\mathbf{P}_d^{(2)}(\Omega)$  is the bulk electric dipole contribution,  $\mathbf{P}_s^{(2)}(\Omega)$  is the surface electric dipole contribution, and  $\mathbf{P}_q^{(2)}(\Omega)$

is the higher-order electric quadrupole contribution. Because both  $(\text{BA})_2\text{PbI}_4$  (orthorhombic,  $Pcba$  space group) and  $(\text{iso-BA})_2\text{PbI}_4$  (monoclinic,  $P2_1/C$  space group) are centrosymmetric, the bulk electric dipole with a nonlinear susceptibility  $\chi_d^{(2)}$  is forbidden. Considering the symmetry can be broken in the near-surface region and the space group will degenerate into species with lower symmetry, a surface electric dipole with a nonlinear susceptibility  $\chi_s^{(2)}$  could contribute to the THz emission of these 2D perovskites. However, the overwhelming evidence of the  $4\varphi$  symmetry in Fig. 5(e) excludes the dominant role of surface electric dipole in  $(\text{BA})_2\text{PbI}_4$  because this symmetry cannot be supported by an electric dipole, even considering the surface electric field. Therefore,

multiple-source polarization must be considered in the THz generation mechanism of  $(\text{BA})_2\text{PbI}_4$ .

Governed by the leading-order response of electric quadrupole, the nonlinear polarization is proportional to the products of the pump electric field  $\mathbf{E}$  and its gradient as [55]

$$\mathbf{P}_{q,i}^{(2)}(\Omega) = \chi_{q,ijkl}^{(2)}(\Omega = \omega - \omega)\mathbf{E}_j\nabla_k\mathbf{E}_l, \quad (2)$$

where the nonlinear susceptibility  $\chi_q^{(2)}$  is a fourth-rank tensor containing 81 elements. For  $(\text{BA})_2\text{PbI}_4$  with an orthorhombic structure, the independent and nonvanishing tensor elements are  $\chi_{q,iiii}^{(2)}$ ,  $\chi_{q,iiij}^{(2)}$ ,  $\chi_{q,ijij}^{(2)}$ , and  $\chi_{q,ijji}^{(2)}$  (in terms of the crystallographic axis with distinct  $i$  and  $j$ ) [54]. To apply Eq. (2), the quantities in the laboratory coordinate should be transformed into the crystal coordinate. The calculation procedure can be found in Appendix A. For the  $p$ -polarized excitation condition with a fixed incident angle of  $-40^\circ$ , the THz radiation from the (001) crystal face can be summarized briefly as [54]

$$E_{\text{THz}} \propto a_1 \cos 4\varphi + b_1 \cos 2\varphi + c_1, \quad (3)$$

where the constants  $a_1$ ,  $b_1$ , and  $c_1$  are determined by the nonlinear susceptibility nonvanishing tensor elements and the angle of light propagation in the medium. Readers can find the detailed forms of  $a_1$ ,  $b_1$ , and  $c_1$  in Appendix A. Data fitting calculation has been carried out by using Eq. (3), and the resulting red line agrees well with the experiment, as shown in Fig. 5(e). The proportion of the cosine and constant terms are represented as three horizontal bars, which originate from the anisotropic and isotropic terms of Eq. (3) due to the same nonlinear source polarization. Furthermore, the incident angle dependence of the THz electric field can be simplified as [56]

$$E_{\text{THz}} \propto d_1 \cos \theta_{\text{THz}} \sin \theta + e_1 \sin \theta_{\text{THz}} \cos \theta, \quad (4)$$

where  $\theta_{\text{THz}} = \sin^{-1}[\sin(\theta)/n_{\text{THz}}]$  is the refraction angle of the generated THz pulses in the sample. Here,  $d_1$  and  $e_1$  are determined by the nonlinear susceptibility tensor elements and a fixed azimuthal angle, as shown in Appendix A. The red line in Fig. 5(a), which agrees well with the incident-angle-dependent experiment, is fitted by Eq. (4). In addition, the dependence of THz radiation on incident linear polarization angle is expressed as

$$E_{\text{THz}} \propto f_1 \sin 2\alpha + g_1 \cos 2\alpha + h_1, \quad (5)$$

where  $f_1$ ,  $g_1$ , and  $h_1$  are determined by the parameter as mentioned above; the detailed forms can be found in the Appendix A. The fitting curve using Eq. (5) agrees well with the experimental data, as shown in Fig. 5(c). As a conclusion, the agreement between experiment and theory confirms that the THz emission from  $(\text{BA})_2\text{PbI}_4$  is driven by electric quadrupole.

In comparison, the anisotropy dependence of THz generation on  $\varphi$  exhibits an obviously low-order symmetry of  $(\text{iso-BA})_2\text{PbI}_4$ , as shown in Fig. 5(f). Therefore, the higher-order multipole source polarization beyond the electric dipole could not play a key role. This result can be attributed to the monoclinic structure of the material, which terminates the multipole expansion at the electric dipole term [57]. Considering the inversion symmetry broken in the near-surface region ( $z \sim z_0$ ), the surface electric dipole polarization density can

be given by

$$\mathbf{P}_{s,i}^{(2)}(\Omega) = \sum_{jk} \chi_{s,ijk}^{(2)}(\Omega = \omega - \omega)\mathbf{E}_j\mathbf{E}_k\delta(z - z_0), \quad (6)$$

where  $\delta$  is a step function response limiting this polarization in the near-surface region. Here, we assume that the point group of  $(\text{iso-BA})_2\text{PbI}_4$  in the near-surface region degenerates from  $C_{2h}$  to  $C_2$  [58,59]. After transforming the quantities from the laboratory coordinate to the crystal coordinate, the azimuthal angle-dependent THz electric field can be simplified as follows:

$$E_{\text{THz}} \propto a_2 \sin \varphi + b_2 \sin 2\varphi + c_2 \sin 3\varphi + d_2, \quad (7)$$

where the parameters  $a_2$ ,  $b_2$ , and  $c_2$  are related to the nonlinear susceptibility tensor elements, as shown in Appendix B. Here,  $d_2$  in Eq. (7) is a background term that does not change with the azimuthal angle. Using Eq. (7), the calculated fitting line in Fig. 5(f) exhibits good agreement with the experiment. Note that the proportion of each item in Eq. (7) is shown in the inset of Fig. 5(f) and suggests a quite different contribution of sinusoidal function with varied symmetries. Except for the constant term, the proportion of  $\sin \varphi$ ,  $\sin 2\varphi$ , and  $\sin 3\varphi$  is  $\sim 17 : 13 : 1$ . The relatively low proportion of the  $\sin 3\varphi$  term implies that the point group of  $(\text{iso-BA})_2\text{PbI}_4$  could partly change to species with lower symmetry than  $C_2$  in the surface region. Moreover, the large proportion of the  $\sin \varphi$  term probably refers a strong electric dipole with an inclination angle to the normal direction, which may result from the monoclinic structure of  $(\text{iso-BA})_2\text{PbI}_4$ . Moreover, the dependence of THz radiation on the incident angle and incident linear polarization angle can be expressed as

$$E_{\text{THz}} \propto \cos \theta_{\text{THz}}(e_2 \cos 2\theta + f_2 \sin 2\theta + g_2) + \sin \theta_{\text{THz}}(h_2 \cos 2\theta + i_2 \sin 2\theta + j_2), \quad (8)$$

$$E_{\text{THz}} \propto k_2 \cos 2\alpha + l_2 \sin 2\alpha + m_2, \quad (9)$$

where the parameters are related to the nonlinear susceptibility tensor elements, as given in Appendix B. The experimental data in Figs. 5(b) and 5(d) can be well fitted by Eqs. (8) and (9), respectively. In conclusion, these results suggest that the THz emission from  $(\text{iso-BA})_2\text{PbI}_4$  is governed by the surface electric dipole-induced optical rectification effect. It is worth noting that the diverse slope values observed in Fig. 4 for  $(\text{BA})_2\text{PbI}_4$  and  $(\text{iso-BA})_2\text{PbI}_4$  can be attributed to the distinct nonlinear source polarization-induced alterations in the nonlinear susceptibility tensors and their dispersion characteristics.

At last, the physical mechanisms of THz generation from  $(\text{BA})_2\text{PbI}_4$  and  $(\text{iso-BA})_2\text{PbI}_4$  are illustrated in Figs. 6(a) and 6(b), respectively. There are both commonalities and differences between the two 2D RPPs. The common feature is that the THz generation is more robust under below-band-gap excitation with the 800 nm laser than that under above-band-gap excitation with the 400 nm laser. Moreover, the linear optical-effect-induced photocurrent, which is reported to be dominant in many traditional THz generation semiconductors and even 3D perovskite  $\text{MAPbI}_3$  [32,33], is excluded from the THz generation mechanisms according to the linear dependence on the pump fluence. Hence, we conclude that the photocurrent perpendicular to the surface of 2D RPPs

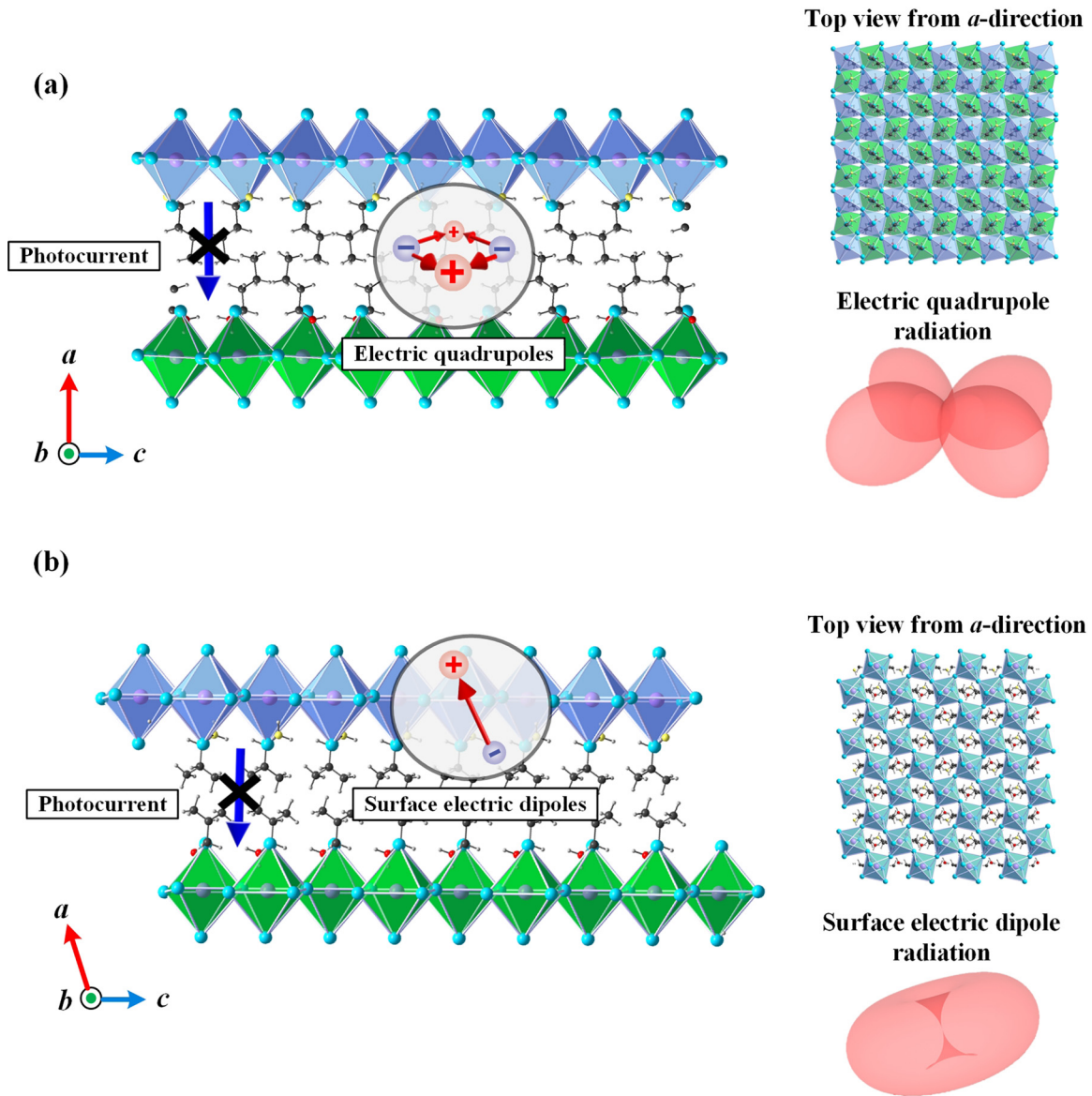


FIG. 6. Schematic illustrations of the terahertz (THz) generation mechanism of (a)  $(\text{BA})_2\text{PbI}_4$  and (b)  $(\text{iso-BA})_2\text{PbI}_4$ . The upper right corner is the top view of the material. The first inorganic layer is shown in blue, and the second layer is shown in green. The lower right corner is the three-dimensional (3D) diagram of the quadrupole or dipole radiation.

is suppressed by their unique structural characteristics. As illustrated in Fig. 6, the multiple-quantum-well structure is constructed with alternant conducting  $[\text{PbI}_6]^{4-}$  layers and insulating organic layers, which are parallel to the surface of the substrate. In the direction perpendicular to the sample surface, the photocurrent between adjacent conductor layers is forbidden by the organic layers. Instead, nonlinear polarization is enhanced largely due to the quantum and dielectric confinement effect [50]. Therefore, the THz generation dominated by nonlinear polarization under below-band-gap excitation is much stronger than that by photocurrent under above-band-gap excitation.

Under below-band-gap excitation, there is still a remarkable difference between the polarization mechanisms for the THz generation from  $(\text{BA})_2\text{PbI}_4$  and  $(\text{iso-BA})_2\text{PbI}_4$ . It is particularly evident in the azimuthal angle-dependent THz

generation results that  $(\text{BA})_2\text{PbI}_4$  exhibits  $4\varphi$  symmetry, while  $(\text{iso-BA})_2\text{PbI}_4$  shows complex low-order symmetry. Although the bulk electric dipole is forbidden in both  $(\text{BA})_2\text{PbI}_4$  and  $(\text{iso-BA})_2\text{PbI}_4$  due to the centrosymmetric structures, the polarization has different sources in these two 2D RPPs. In  $(\text{BA})_2\text{PbI}_4$ , the  $4\varphi$  symmetry indicates the electric quadrupole effect with higher order than the bulk electric dipole. The emergence of the electric quadrupole contribution may be related to the orthorhombic structure, which has been reported to govern the THz generation of orthorhombic  $\text{YBa}_2\text{Cu}_3\text{O}_{7-\delta}$  [56]. As shown in the upper right corner of Fig. 6(a), the inorganic layer in  $(\text{BA})_2\text{PbI}_4$  is a staggered configuration, the lead atoms can be offset in each adjacent layer, and every second layer is eclipsed [60]. This staggered structure provides an offset between the two dipoles, thus allowing for the existence of a quadrupole. Moreover, the discontinuity

of the electric field in the normal direction could give rise to a large gradient that can support a sizeable contribution from higher-order multipole terms [61]. In comparison, the low-order symmetry of (iso-BA)<sub>2</sub>PbI<sub>4</sub> suggests a dominant role of surface electric dipole. The largest proportion is the  $\sin\varphi$  term according to the fitting parameters. This result could be related to the monoclinic structure of (iso-BA)<sub>2</sub>PbI<sub>4</sub> [62]. The upper right corner of Fig. 6(b) shows the inorganic layer in (iso-BA)<sub>2</sub>PbI<sub>4</sub> is an eclipsed configuration; the lead atoms can be directly above each other in each adjacent layer. This eclipsed structure does not satisfy the conditions for the existence of quadrupoles. Moreover, the monoclinic structure has a nonorthogonal axial direction, as illustrated in lower right corner of Fig. 6(b). The total effect is close to the dominant role of an oblique surface electric dipole radiation.

#### IV. CONCLUSIONS

The carrier dynamics and nonlinear polarization mechanisms of (BA)<sub>2</sub>PbI<sub>4</sub> and (iso-BA)<sub>2</sub>PbI<sub>4</sub> are investigated by THz emission spectroscopy. Under above-band-gap excitation, the THz emission shows a linear dependence on the pump fluence, indicating the dominant role of shift current induced by a second-order nonlinear effect instead of linear photocurrents, which is perpendicular to the sample surface and significant in 3D perovskites and many other conventional semiconductors. Moreover, remarkable enhancement of the THz amplitude under below-band-gap excitation is observed, demonstrating that the nonlinear polarization is more greatly strengthened than photocurrents in 2D perovskite, and the THz generation mechanism can be attributed to the optical rectification effect. The suppressed out-of-plane photocurrents and enhanced nonlinear polarization could be induced by the unique multiple-quantum-well structure of 2D perovskites. According to the dependence of THz amplitude on the incident angle, polarization angle of the pump laser, and azimuthal angle, it can be inferred that the nonlinear polarization originates from different polarization source terms in (BA)<sub>2</sub>PbI<sub>4</sub> and (iso-BA)<sub>2</sub>PbI<sub>4</sub>. For (BA)<sub>2</sub>PbI<sub>4</sub> crystallized in the orthorhombic system, the polarization comes from the higher-order electric quadrupole term instead of the forbidden bulk electric dipole term, thus leading to a remarkable  $4\varphi$  symmetry. For (iso-BA)<sub>2</sub>PbI<sub>4</sub> crystallized in the monoclinic system, the surface electric dipole may govern the polarization and induce a low-order  $\varphi$  symmetry of the THz generation. These results provide insight into the carrier transport and nonlinear polarization mechanisms in 2D perovskites by understanding the THz generation mechanisms deeply, which is

also essential for the design of 2D perovskite-based optoelectrical applications.

#### ACKNOWLEDGMENTS

This paper was supported by National Natural Science Foundation of China (Grants No. 11974279, No. 12074311, No. 12261141662, and No. 12004310).

The authors declare no competing financial interest.

#### APPENDIX A: CALCULATION OF THE NONLINEAR POLARIZATION AND THz ELECTRIC FIELD OF (BA)<sub>2</sub>PbI<sub>4</sub> DRIVEN BY ELECTRIC QUADRUPOLE

The incident electric field  $\mathbf{E}$  is projected onto the  $xyz$  crystal coordinate system; herein, the incident electric field components in three directions can be given as

$$\begin{aligned} E_x &= \cos\alpha \sin\theta E_0 \\ E_y &= \sin\alpha E_0 \\ E_z &= \cos\alpha \cos\theta E_0. \end{aligned} \quad (\text{A1})$$

The nonlinear dielectric polarization components are proportional to the products of the pump electric field  $\mathbf{E}$  and its gradient; the formula is shown as

$$\mathbf{P}_{q,i}^{(2)}(\Omega) = \sum_{j,k,l} \chi_{q,ijkl}^{(2)}(\Omega = \omega - \omega) \mathbf{E}_j \nabla_k \mathbf{E}_l, \quad (\text{A2})$$

where the nonlinear susceptibility  $\chi_q^{(2)}$  is a fourth-rank tensor containing 81 elements. For (BA)<sub>2</sub>PbI<sub>4</sub> with an orthorhombic structure, the independent and nonvanishing tensor elements are  $\chi_{q,iii}^{(2)}$ ,  $\chi_{q,ii,jj}^{(2)}$ ,  $\chi_{q,ij,ij}^{(2)}$ , and  $\chi_{q,ij,ji}^{(2)}$  (in terms of the crystallographic axis with distinct  $i$  and  $j$ ).

In the experiment, the sample holder can be rotated around the  $z$  axis in a set of azimuthal angles, and we can obtain the transformed tensor containing azimuthal angle via a rotating operation  $\mathbf{R}(\varphi)$ :

$$\mathbf{R}(\varphi) = \begin{bmatrix} \cos\varphi & \sin\varphi & 0 \\ -\sin\varphi & \cos\varphi & 0 \\ 0 & 0 & 1 \end{bmatrix}. \quad (\text{A3})$$

The susceptibility elements can be calculated according to the calculation law of high-order tensors as follows:

$$\chi_{i_1, i_2 \dots i_{n+1}}^{(n)} = \sum_{j_1, j_2 \dots j_{n+1}} T_{i_1, j_1} T_{i_2, j_2} \dots T_{i_{n+1}, j_{n+1}} \chi_{j_1, j_2 \dots j_{n+1}}^{(n)}. \quad (\text{A4})$$

The nonlinear dielectric polarization components can be obtained as follows:

$$\begin{aligned} P_x &= -\frac{1}{4} \sin 2\theta \sin 2\alpha E_0^2 (\chi_{xxzz} \cos^2\varphi + \chi_{yyzz} \sin^2\varphi) + \sin\theta \cos^2\alpha E_0^2 [\chi_{xxyy} \cos^4\varphi + \chi_{yyxx} \sin^4\varphi \\ &\quad + (\chi_{xxxx} + \chi_{yyyy} - \chi_{xyxy} - \chi_{yyxx} - \chi_{xyyx} - \chi_{yyxy}) \cos^2\varphi \sin^2\varphi] \\ &\quad - \frac{1}{2} \sin^2\theta \sin 2\alpha E_0^2 [\chi_{xxxx} \cos^4\varphi + \chi_{yyyy} \sin^4\varphi + (\chi_{xxyy} + \chi_{xyxy} + \chi_{yyxx} + \chi_{xyyx} + \chi_{yyxy} + \chi_{yyxx}) \cos^2\varphi \sin^2\varphi], \\ P_y &= -\sin\theta \sin^2\alpha E_0^2 [\chi_{xxyy} \sin^4\varphi + \chi_{yyxx} \cos^4\varphi + (\chi_{xxxx} + \chi_{yyyy} - \chi_{xyxy} - \chi_{yyxx} - \chi_{xyyx} - \chi_{yyxy}) \cos^2\varphi \sin^2\varphi] \\ &\quad + \frac{1}{2} \sin 2\alpha E_0^2 [\chi_{xxxx} \sin^4\varphi + \chi_{yyyy} \cos^4\varphi + (\chi_{xxyy} + \chi_{xyxy} + \chi_{yyxx} + \chi_{xyyx} + \chi_{yyxy} + \chi_{yyxx}) \cos^2\varphi \sin^2\varphi] \\ &\quad - \cos\theta \sin^2\alpha E_0^2 (\chi_{xxzz} \sin^2\varphi + \chi_{yyzz} \cos^2\varphi), \end{aligned}$$

$$P_z = -\frac{1}{4} \sin 2\alpha \sin 2\theta E_0^2 (\chi_{zzyy} \sin^2 \varphi + \chi_{zzxx} \cos^2 \varphi) + \cos \theta \cos^2 \alpha E_0^2 (\chi_{zzxx} \sin^2 \varphi + \chi_{zzyy} \cos^2 \varphi) - \frac{1}{2} \cos^2 \theta \sin 2\alpha E_0^2 \chi_{zzzz}. \quad (\text{A5})$$

The amplitude of generated THz radiation is proportional to nonlinear dielectric polarization, and it can be expressed as

$$E_{\text{THz}} \propto P_x \cos \theta_{\text{THz}} - P_z \sin \theta_{\text{THz}}, \quad (\text{A6})$$

where  $\theta_{\text{THz}} = \sin^{-1}[\sin(\theta)/n_{\text{THz}}]$  is the refraction angle of the generated THz pulses in the material. Here,  $n_{\text{THz}}$  are the refractive indices of the infrared and THz pulses propagating inside the sample. Therefore, the dependence of THz electric field amplitude on the azimuthal, incident, and polarization angles can be calculated.

The azimuthal angle dependence under  $p$ -polarized light ( $\alpha = 0$ ) excitation is as follows:

$$E_{\text{THz}} \propto a_1 \cos 4\varphi + b_1 \cos 2\varphi + c_1, \quad (\text{A7})$$

where fitting coefficients  $a_1$ ,  $b_1$ , and  $c_1$  are related to nonlinear susceptibility tensor elements and  $\theta$  is the fixed incidence angle. The specific parameters are as follows:

$$\begin{aligned} a_1 &= \frac{1}{8} \cos \theta_{\text{THz}} \sin \theta (\chi_{xxyy} + \chi_{yyxx} + \chi_{xyxy} + \chi_{xyyx} + \chi_{yxyx} + \chi_{yxxy} - \chi_{xxxx} - \chi_{yyyy}), \\ b_1 &= \frac{1}{2} \cos \theta_{\text{THz}} \sin \theta (\chi_{xxyy} - \chi_{yyxx}) + \frac{1}{2} \sin \theta_{\text{THz}} \cos \theta (\chi_{zzxx} - \chi_{zzyy}), \\ c_1 &= \frac{3}{8} \cos \theta_{\text{THz}} \sin \theta [\chi_{xxyy} + \chi_{yyxx} + \frac{2}{3} (\chi_{xxxx} + \chi_{yyyy} - \chi_{xyxy} - \chi_{xyyx} - \chi_{yxyx} - \chi_{yxxy}) \\ &\quad + \frac{1}{3} (\chi_{xyxy} + \chi_{xyyx} + \chi_{yxyx} + \chi_{yxxy} - \chi_{xxxx} - \chi_{yyyy})] - \frac{1}{2} \sin \theta_{\text{THz}} \cos \theta (\chi_{zzxx} - \chi_{zzyy}). \end{aligned} \quad (\text{A8})$$

The incident angle dependence of the THz electric field amplitude can be simplified as

$$E_{\text{THz}} \propto d_1 \cos \theta_{\text{THz}} \sin \theta + e_1 \sin \theta_{\text{THz}} \cos \theta, \quad (\text{A9})$$

where the fitting coefficients  $d_1$  and  $e_1$  are related to nonlinear susceptibility coefficients and a fixed azimuthal angle. The details are given by

$$\begin{aligned} d_1 &= E_0^2 [\chi_{xxyy} \cos^4 \varphi + \chi_{yyxx} \sin^4 \varphi + (\chi_{xxxx} + \chi_{yyyy} - \chi_{xyxy} - \chi_{xyyx} - \chi_{yxyx} - \chi_{yxxy}) \cos^2 \varphi \sin^2 \varphi], \\ e_1 &= -E_0^2 (\chi_{zzxx} \sin^2 \varphi + \chi_{zzyy} \cos^2 \varphi). \end{aligned} \quad (\text{A10})$$

The dependence of THz radiation on the incident linear polarization angle is expressed as

$$E_{\text{THz}} \propto f_1 \sin 2\alpha + g_1 \cos 2\alpha + h_1, \quad (\text{A11})$$

where  $f_1$ ,  $g_1$ , and  $h_1$  are determined by the parameter as mentioned above. The detailed forms are shown as follows:

$$\begin{aligned} f_1 &= \cos \theta_{\text{THz}} \left\{ -\frac{1}{4} \sin 2\theta E_0^2 (\chi_{xxzz} \cos^2 \varphi + \chi_{yyzz} \sin^2 \varphi) - \frac{1}{2} \sin^2 \theta E_0^2 [\chi_{xxxx} \cos^4 \varphi + \chi_{yyyy} \sin^4 \varphi \right. \\ &\quad \left. + (\chi_{xxyy} + \chi_{xyxy} + \chi_{yyxx} + \chi_{xyyx} + \chi_{yxyx} + \chi_{yxxy}) \cos^2 \varphi \sin^2 \varphi \right\} \\ &\quad + \sin \theta_{\text{THz}} \left[ \frac{1}{4} \sin 2\theta E_0^2 (\chi_{zzyy} \sin^2 \varphi + \chi_{zzxx} \cos^2 \varphi) + \frac{1}{2} \cos^2 \theta E_0^2 \chi_{zzzz} \right], \\ g_1 &= \frac{1}{2} \cos \theta_{\text{THz}} \sin \theta E_0^2 [\chi_{xxyy} \cos^4 \varphi + \chi_{yyxx} \sin^4 \varphi + (\chi_{xxxx} + \chi_{yyyy} - \chi_{xyxy} - \chi_{xyyx} - \chi_{yxyx} - \chi_{yxxy}) \cos^2 \varphi \sin^2 \varphi] \\ &\quad - \frac{1}{2} \sin \theta_{\text{THz}} \cos \theta E_0^2 (\chi_{zzxx} \sin^2 \varphi + \chi_{zzyy} \cos^2 \varphi), \\ h_1 &= \frac{1}{2} \cos \theta_{\text{THz}} \sin \theta E_0^2 [\chi_{xxyy} \cos^4 \varphi + \chi_{yyxx} \sin^4 \varphi + (\chi_{xxxx} + \chi_{yyyy} - \chi_{xyxy} - \chi_{xyyx} - \chi_{yxyx} - \chi_{yxxy}) \cos^2 \varphi \sin^2 \varphi] \\ &\quad - \frac{1}{2} \sin \theta_{\text{THz}} \cos \theta E_0^2 (\chi_{zzxx} \sin^2 \varphi + \chi_{zzyy} \cos^2 \varphi). \end{aligned} \quad (\text{A12})$$

## APPENDIX B: CALCULATION OF THE NONLINEAR POLARIZATION AND THz ELECTRIC FIELD OF (iso-BA)<sub>2</sub>PbI<sub>4</sub> DRIVEN BY SURFACE ELECTRIC DIPOLE

The point group on the surface of a (iso-BA)<sub>2</sub>PbI<sub>4</sub> single crystal becomes  $C_2$  after the central symmetry is broken, which determines the susceptibility tensor as follows:

$$\chi_{ijk} = \begin{bmatrix} 0 & 0 & 0 & \chi_{xyz} & \chi_{xzy} & 0 & 0 & \chi_{xxy} & \chi_{xyx} \\ \chi_{yxx} & \chi_{yyy} & \chi_{yzz} & 0 & 0 & \chi_{yzx} & \chi_{yxz} & 0 & 0 \\ 0 & 0 & 0 & \chi_{zyz} & \chi_{zzy} & 0 & 0 & \chi_{zxy} & \chi_{zyx} \end{bmatrix}. \quad (\text{B1})$$

The susceptibility elements containing an azimuthal angle can be calculated according to Eq. (A4), and the surface electric dipole polarization density can be given by

$$\mathbf{P}_{s,i}^{(2)}(\Omega) = \sum_{jk} \chi_{s,ijk}^{(2)}(\Omega = \omega - \omega)\mathbf{E}_j\mathbf{E}_k\delta(z - z_0). \quad (\text{B2})$$

The nonlinear dielectric polarization intensity components along three directions can be obtained as follows:

$$\begin{aligned} P_x &= \frac{1}{2}\varepsilon_0 E_0^2 \{ \sin 2\alpha \cos \theta [\chi_{xyz} - \chi_{yxz} + (\chi_{xyz} + \chi_{yxz}) \cos 2\varphi] + 2\chi_{yzz} \cos^2 a \cos^2 \theta \sin \varphi \\ &\quad + \sin 2\alpha \sin \theta \cos \varphi [\chi_{yyy} - \chi_{yxx} + (2\chi_{xxy} + \chi_{yxx} - \chi_{yyy}) \cos 2\varphi] \\ &\quad + \cos^2 a \sin^2 \theta \sin \varphi [2\chi_{xxy} + \chi_{yxx} + \chi_{yyy} + (2\chi_{xxy} + \chi_{yxx} - \chi_{yyy}) \cos 2\varphi] \\ &\quad + \sin^2 a \sin \varphi [-2\chi_{xxy} + \chi_{yxx} + \chi_{yyy} + (-2\chi_{xxy} - \chi_{yxx} + \chi_{yyy}) \cos 2\varphi] + \cos^2 a \sin 2\theta \sin 2\varphi (\chi_{xyz} + \chi_{yxz}), \\ P_y &= \frac{1}{4}\varepsilon_0 E_0^2 \{ 4\chi_{yzz} \cos^2 \theta \cos^2 a \cos \varphi + 2\cos^2 a \cos \varphi \sin^2 \theta [-2\chi_{xxy} + \chi_{yxx} + \chi_{yyy} + (2\chi_{xxy} + \chi_{yxx} - \chi_{yyy}) \cos 2\varphi] \\ &\quad + 2\cos^2 a \sin 2\theta [-\chi_{xyz} + \chi_{yxz} + (\chi_{xyz} + \chi_{yxz}) \cos 2\varphi] \\ &\quad + \sin^2 a [(2\chi_{xxy} + \chi_{yxx} + 3\chi_{yyy}) \cos \varphi + (-2\chi_{xxy} - \chi_{yxx} + \chi_{yyy}) \cos 3\varphi] \\ &\quad - 2 \sin 2\alpha \sin \theta \sin \varphi [\chi_{yxx} - \chi_{yyy} + (2\chi_{xxy} + \chi_{yxx} - \chi_{yyy}) \cos 2\varphi] - 2 \sin 2\alpha \cos \theta \sin 2\varphi (\chi_{xyz} + \chi_{yxz}), \\ P_z &= \varepsilon_0 E_0^2 [\chi_{zyz} \sin 2\alpha \cos \theta \cos \varphi + \chi_{zxy} \cos 2\varphi \sin 2\alpha \sin \theta + \chi_{zyz} \cos^2 a \sin 2\theta \sin \varphi + \chi_{zxy} \sin 2\varphi (\cos^2 a \sin^2 \theta - \sin^2 a)]. \end{aligned} \quad (\text{B3})$$

The amplitude of the generated THz electric field can be expressed as

$$E_{\text{THz}} \propto P_x \cos \theta_{\text{THz}} - P_z \sin \theta_{\text{THz}}. \quad (\text{B4})$$

The azimuthal dependence under  $p$ -polarized light ( $\alpha = 0$ ) excitation is as follows:

$$E_{\text{THz}} \propto a_2 \sin \varphi + b_2 \sin 2\varphi + c_2 \sin 3\varphi + d_2. \quad (\text{B5})$$

The constant  $d_2$  represents the azimuth-independence background contribution. The fitting coefficients  $a_2$ ,  $b_2$ , and  $c_2$  are related to nonlinear susceptibility tensor elements and the angle of light propagation in the medium:

$$\begin{aligned} a_2 &= \varepsilon_0 E_0^2 \cos \theta_{\text{THz}} [2\cos^2 \theta \chi_{yzz} + \frac{1}{2}\sin^2 \theta (2\chi_{xxy} + \chi_{yxx} + 3\chi_{yyy})] - 2\varepsilon_0 E_0^2 \sin \theta_{\text{THz}} \sin 2\theta \chi_{zyz}, \\ b_2 &= \varepsilon_0 E_0^2 \cos \theta_{\text{THz}} \sin 2\theta (\chi_{xyz} + \chi_{yxz}) - 2\varepsilon_0 E_0^2 \sin \theta_{\text{THz}} \sin^2 \theta \chi_{zxy}, \\ c_2 &= \frac{1}{2}\varepsilon_0 E_0^2 \cos \theta_{\text{THz}} (2\chi_{xxy} + \chi_{yxx} - \chi_{yyy}) \sin^2 \theta. \end{aligned} \quad (\text{B6})$$

The formula of the THz amplitude from (iso-BA)<sub>2</sub>PbI<sub>4</sub> as a function of incident angle can be expressed as

$$E_{\text{THz}} \propto \cos \theta_{\text{THz}} (e_2 \cos 2\theta + f_2 \sin 2\theta + g_2) + \sin \theta_{\text{THz}} (h_2 \cos 2\theta + i_2 \sin 2\theta + j_2), \quad (\text{B7})$$

where the parameters are related to the nonlinear susceptibility tensor elements and a fixed azimuthal angle. The detailed forms are shown as

$$\begin{aligned} e_2 &= \frac{1}{4}E_0^2 \{ 2\chi_{yzz} \sin \varphi + \sin \varphi [2\chi_{xxy} + \chi_{yxx} + \chi_{yyy} + (2\chi_{xxy} + \chi_{yxx} - \chi_{yyy}) \cos 2\varphi] \}, \quad f_2 = \frac{1}{2}E_0^2 \sin 2\varphi (\chi_{xyz} + \chi_{yxz}), \\ g_2 &= \frac{1}{4}E_0^2 \sin \varphi \{ 2\chi_{yzz} + \cos 2\varphi [2\chi_{xxy} + \chi_{yxx} + \chi_{yyy} + (2\chi_{xxy} + \chi_{yxx} - \chi_{yyy})] \}, \\ h_2 &= \frac{1}{2}E_0^2 \chi_{zxy} \sin 2\varphi, \quad i_2 = -E_0^2 \chi_{zyz} \sin \varphi, \quad j_2 = -\frac{1}{2}E_0^2 \chi_{zxy} \sin 2\varphi. \end{aligned} \quad (\text{B8})$$

The dependence of THz radiation on incident linear polarization angle is expressed as

$$E_{\text{THz}} \propto k_2 \cos 2\alpha + l_2 \sin 2\alpha + m_2, \quad (\text{B9})$$

where  $k_1$ ,  $l_1$ , and  $m_1$  shown as

$$\begin{aligned} k_2 &= \frac{1}{4}E_0^2 \cos \theta_{\text{THz}} \{ 2\chi_{yzz} \cos^2 \theta \sin \varphi + \sin 2\theta \sin 2\varphi (\chi_{xyz} + \chi_{yxz}) + \sin^2 \theta \sin \varphi [2\chi_{xxy} + \chi_{yxx} + \chi_{yyy} \\ &\quad + (2\chi_{xxy} + \chi_{yzz} - \chi_{yyy}) \cos 2\varphi] + \sin \varphi [-2\chi_{xxy} + \chi_{yxx} + \chi_{yyy} + (-2\chi_{xxy} - \chi_{yxx} + \chi_{yyy}) \cos 2\varphi] \\ &\quad - \frac{1}{2} \sin \theta_{\text{THz}} E_0^2 [\chi_{zyz} \sin 2\theta \sin \varphi + \chi_{zxy} \sin 2\varphi (\sin^2 \theta + 1)], \\ l_2 &= \frac{1}{2}E_0^2 \cos \theta_{\text{THz}} \{ \cos \theta [\chi_{xyz} - \chi_{yxz} + \cos 2\varphi (\chi_{xyz} + \chi_{yxz})] + \sin \theta \cos \varphi [\chi_{yyy} - \chi_{yxx} + \cos 2\varphi (2\chi_{xxy} + \chi_{yxx} - \chi_{yyy})] \} \\ &\quad - \sin \theta_{\text{THz}} E_0^2 (\chi_{zyz} \cos \theta \cos \varphi + \chi_{zxy} \cos 2\varphi \sin \theta). \\ m_2 &= \frac{1}{4}E_0^2 \cos \theta_{\text{THz}} \{ 2\chi_{yzz} \cos^2 \theta \sin \varphi + \sin 2\theta \sin 2\varphi (\chi_{xyz} + \chi_{yxz}) \\ &\quad + \sin^2 \theta \sin \varphi [2\chi_{xxy} + \chi_{yxx} + \chi_{yyy} + (2\chi_{xxy} + \chi_{yxx} - \chi_{yyy}) \cos 2\varphi] \} \end{aligned}$$

$$\begin{aligned}
& + \sin \varphi [-2\chi_{xy} + \chi_{yx} + \chi_{yy} + (-2\chi_{xy} - \chi_{yx} + \chi_{yy}) \cos 2\varphi] \\
& - \frac{1}{2} \sin \theta_{\text{THz}} E_0^2 [\chi_{yz} \sin 2\theta \sin \varphi + \chi_{xy} \sin 2\varphi (\sin^2 \theta - 1)].
\end{aligned}
\tag{B10}$$

- 
- [1] Y. T. Chan, N. Elliger, B. Klis, M. Kollár, E. Horváth, L. Forró, M. Dressel, and E. Uykur, *Phys. Rev. B* **106**, 214106 (2022).
- [2] F. Zhang, S. Y. Park, C. Yao, H. Lu, S. P. Dunfield, C. Xiao, S. Ulicna, X. Zhao, L. Du Hill, and X. Chen, *Science* **375**, 71 (2022).
- [3] J. Tong, Q. Jiang, A. J. Ferguson, A. F. Palmstrom, X. Wang, J. Hao, S. P. Dunfield, A. E. Louks, S. P. Harvey, and C. Li, *Nat. Energy* **7**, 642 (2022).
- [4] X. Gao, X. Zhang, W. Yin, H. Wang, Y. Hu, Q. Zhang, Z. Shi, V. L. Colvin, W. W. Yu, and Y. Zhang, *Adv. Sci.* **6**, 1900941 (2019).
- [5] R. L. Milot, R. J. Sutton, G. E. Eperon, A. A. Haghighirad, J. Martinez Hardigree, L. Miranda, H. J. Snaith, M. B. Johnston, and L. M. Herz, *Nano Lett.* **16**, 7001 (2016).
- [6] K. Leng, I. Abdelwahab, I. Verzhbitskiy, M. Telychko, L. Chu, W. Fu, X. Chi, N. Guo, Z. Chen, and Z. Chen, *Nat. Mater.* **17**, 908 (2018).
- [7] C. C. Stoumpos, D. H. Cao, D. J. Clark, J. Young, J. M. Rondinelli, J. I. Jang, J. T. Hupp, and M. G. Kanatzidis, *Chem. Mater.* **28**, 2852 (2016).
- [8] E. Amerling, S. Baniya, E. Lafalce, C. Zhang, Z. V. Vardeny, and L. Whittaker-Brooks, *J. Phys. Chem. Lett.* **8**, 4557 (2017).
- [9] D. Wang, B. Wen, Y. N. Zhu, C. J. Tong, Z. K. Tang, and L. M. Liu, *J. Phys. Chem. Lett.* **8**, 876 (2017).
- [10] K. Tanaka, T. Takahashi, T. Kondo, K. Umeda, K. Ema, T. Umabayashi, K. Asai, K. Uchida, and N. Miura, *Jpn. J. Appl. Phys.* **44**, 5923 (2005).
- [11] O. Yaffe, A. Chernikov, Z. M. Norman, Y. Zhong, A. Velauthapillai, A. van der Zande, J. S. Owen, and T. F. Heinz, *Phys. Rev. B* **92**, 045414 (2015).
- [12] J. Du, M. Zhang, and J. Tian, *Int. J. Miner. Metall. Materi.* **29**, 49 (2022).
- [13] Y. Chen, Y. Sun, J. Peng, W. Zhang, X. Su, K. Zheng, T. Pullerits, and Z. Liang, *Adv. Energy Mater.* **7**, 1700162 (2017).
- [14] K. Wang, C. Wu, D. Yang, Y. Jiang, and S. Priya, *ACS Nano* **12**, 4919 (2018).
- [15] L. Xu, Y. Qiang, H. Hu, P. Lin, P. Wang, S. Che, H. Sun, Z. Nie, C. Cui, F. Wu *et al.*, *Nanotechnology* **30**, 105703 (2019).
- [16] J.-Y. Seo, J. Choi, H.-S. Kim, J. Kim, J.-M. Yang, C. Cuhadar, J. S. Han, S.-J. Kim, D. Lee, H. W. Jang *et al.*, *Nanoscale* **9**, 15278 (2017).
- [17] Y. Chen, Y. Sun, J. Peng, J. Tang, K. Zheng, and Z. Liang, *Adv. Mater.* **30**, 1703487 (2018).
- [18] L. Li, L. Jin, Y. Zhou, J. Li, J. Ma, S. Wang, W. Li, and D. Li, *Adv. Optical Mater.* **7**, 1900988 (2019).
- [19] X. Hong, T. Ishihara, and A. V. Nurmikko, *Phys. Rev. B* **45**, 6961 (1992).
- [20] T. Ishihara, J. Takahashi, and T. Goto, *Phys. Rev. B* **42**, 11099 (1990).
- [21] A. Ghribi, R. Ben Aich, K. Boujdaria, T. Barisien, L. Legrand, M. Chamarro, and C. Testelin, *Nanomaterials* **11**, 3054 (2021).
- [22] R. Chakraborty, G. Paul, and A. J. Pal, *Phys. Rev. Appl.* **17**, 054045 (2022).
- [23] X. X. Zhu, H. X. Xu, Y. T. Liu, J. Zhang, M. S. Wang, I. N. Ivanov, O. S. Ovchinnikova, and B. Hu, *Adv. Mater.* **31**, 1901240 (2019).
- [24] X. H. Li, W. W. Liu, Y. Gao, Y. Qin, H. Long, K. Wang, B. Wang, and P. X. Lu, *Opt. Express* **30**, 21094 (2022).
- [25] F. Zhou, I. Abdelwahab, K. Leng, K. P. Loh, and W. Ji, *Adv. Mater.* **31**, 1904155 (2019).
- [26] L. J. Guo, X. Liu, R. D. Cong, L. J. Gao, K. Zhang, L. Zhao, X. Z. Wang, R. N. Wang, C. F. Pan, and Z. Yang, *Nano Lett.* **22**, 8241 (2022).
- [27] Y. Gao, G. Walters, Y. Qin, B. Chen, Y. Min, A. Seifitokaldani, B. Sun, P. Todorovic, M. I. Saidaminov, A. Lough *et al.*, *Adv. Mater.* **31**, 1808336 (2019).
- [28] G. Grinblat, I. Abdelwahab, M. P. Nielsen, P. Dichtl, K. Leng, R. F. Oulton, K. P. Loh, and S. A. Maier, *ACS Nano* **13**, 9504 (2019).
- [29] R. W. Boyd, *Nonlinear Optics* (Academic Press, Boston, 1992).
- [30] T. F. Heinz, *Nonlinear Surface Electromagnetic Phenomena* (Elsevier Science, Amsterdam, 1991).
- [31] X. C. Zhang and D. H. Auston, *J. Appl. Phys.* **71**, 326 (1992).
- [32] B. Guzelurk, R. A. Belisle, M. Smith, K. Bruening, R. Prasanna, Y. Yuan, V. Gopalan, C. J. Tassone, H. I. Karunadasa, and M. McGehee, *Adv. Mater.* **30**, 1704737 (2018).
- [33] C. S. Ponceca, A. Arlauskas, H. Yu, F. Wang, I. Nevinskas, E. Duda, V. Vaicaitis, J. Eriksson, J. Bergqvist, X. K. Liu *et al.*, *ACS Photonics* **6**, 1175 (2019).
- [34] X. Yue, C. Wang, B. Zhang, Z. Zhang, Z. Xiong, X. Zu, Z. Liu, Z. Hu, G. O. Odunmbaku, Y. Zheng *et al.*, *Nat. Commun.* **14**, 917 (2023).
- [35] P. A. Obratsov, D. Lyashenko, P. A. Chizhov, K. Konishi, N. Nemoto, M. Kuwata-Gonokami, E. Welch, A. N. Obratsov, and A. Zakhidov, *Commun. Phys.* **1**, 14 (2018).
- [36] D. Cheng, Z. Liu, L. Luo, C. Vaswani, J. M. Park, Y. Yao, Z. Song, C. Huang, D. H. Mudiyansele, R. H. J. Kim *et al.*, *J. Chem. Phys.* **151**, 244706 (2019).
- [37] Y. He, R. Su, Y. Huang, Y. Zhou, Q. Zhao, J. B. Khurgin, Q. Xiong, and X. Xu, *Adv. Funct. Mater.* **29**, 1904694 (2019).
- [38] Y. He, R. Su, Y. Huang, Q. Zhao, Y. Zhou, J. B. Khurgin, Q. Xiong, and X. Xu, *Adv. Optical Mater.* **9**, 2100822 (2021).
- [39] X. Liu, A. Chanana, U. Huynh, F. Xue, P. Haney, S. Blair, X. Jiang, and Z. Vardeny, *Nat. Commun.* **11**, 323 (2020).
- [40] S. Wang, J. Ma, W. Li, J. Wang, H. Wang, H. Shen, J. Li, J. Wang, H. Luo, and D. Li, *J. Phys. Chem. Lett.* **10**, 2546 (2019).
- [41] See Supplemental Material at <http://link.aps.org/supplemental/10.1103/PhysRevB.108.245403> for more experimental results.
- [42] L. Dou, A. B. Wong, Y. Yi, M. Lai, and P. Yang, *Science* **349**, 1518 (2015).
- [43] C. Fang, M. Xu, J. Ma, J. Wang, L. Jin, M. Xu, and D. Li, *Nano Lett.* **20**, 2339 (2020).
- [44] T. Sheikh, V. Nawale, N. Pathoor, C. Phadnis, A. Chowdhury, and A. Nag, *Angew. Chem. Int. Ed.* **59**, 11653 (2020).
- [45] T. Sheikh, A. Shinde, S. Mahamuni, and A. Nag, *Mater. Res. Express* **6**, 124002 (2019).

- [46] W. Li, J. Ma, H. Wang, C. Fang, and D. Li, *Nanophotonics* **9**, 2001 (2020).
- [47] V. L. Malevich, R. Adomavičius, and A. Krotkus., *C. R. Physique* **9**, 130 (2008).
- [48] L. Zhang, Y. Huang, L. Zhu, Z. Yao, Q. Zhao, W. Du, Y. He, and X. Xu, *Adv. Optical Mater.* **7**, 1801314 (2019).
- [49] J. Dong, K. P. Gradwohl, Y. Xu, T. Wang, B. Zhang, B. Xiao, C. Teichert, and W. Jie, *Photonics Res.* **7**, 518 (2019).
- [50] M. E. Kamminga, H.-H. Fang, M. R. Filip, F. Giustino, J. Baas, G. R. Blake, M. A. Loi, and T. T. M. Palstra, *Chem. Mater.* **28**, 4554 (2016).
- [51] L. Zhu, Y. Huang, C. He, Y. Wu, Y. Zhou, Z. Fan, J. Dong, K. Zhang, and X. Xu, *Phys. Status Solidi RRL* **15**, 2100413 (2021).
- [52] Y. Huang, L. Zhu, Q. Zhao, Y. Guo, Z. Ren, J. Bai, and X. Xu, *ACS Appl. Mater. Interfaces* **9**, 4956 (2017).
- [53] Z. Lei, Y. Huang, Z. Fan, W. Du, C. He, H. Wang, Y. Jin, and X. Xu, *Appl. Phys. Lett.* **116**, 161901 (2020).
- [54] T. F. Heinz, *Nonlinear Surface Electromagnetic Phenomena* (Elsevier Science, Amsterdam, 1991), pp. 360.
- [55] T. A. Germer, K. W. Kołasiński, J. C. Stephenson, and L. J. Richter, *Phys. Rev. B* **55**, 10694 (1997).
- [56] J. L. W. Siders, S. A. Trugman, F. H. Garzon, R. J. Houlton, and A. J. Taylor, *Phys. Rev. B* **61**, 13633 (2000).
- [57] E. B. Graham and R. E. Raab, *Proc. R. Soc. Lond. A* **430**, 593 (1990).
- [58] M. W. Roy, *Symmetry: An Introduction to Group Theory and Its Applications* (Pergamon, Oxford, 1963).
- [59] F. A. Cotton, *Chemical Applications of Group Theory* (Wiley-Interscience, New York, 1990).
- [60] D. G. Billing and A. Lemmerer, *CrystEngComm* **8**, 686 (2006).
- [61] J. E. Sipe, D. J. Moss, and H. M. van Driel, *Phys. Rev. B* **35**, 1129 (1987).
- [62] I. W. H. Oswald, A. A. Koegel, and J. R. Neilson, *Chem. Mater.* **30**, 8606 (2018).